Macromolecules **1998,** *31,* 5441−5449

Investigation of Morphologies of One- and Two-Phase Blends of Isotactic Poly(propene) with Random Poly(ethene-*co*-1-butene)

Y. Thomann, J. Suhm, R. Thomann, G. Bar,* R.-D. Maier, and R. Mülhaupt

Freiburger Materialforschungszentrum and Institut für Makromolekulare Chemie,
Albert-Ludwigs-Universiät Freiburg, Stefan-Meier-Strasse 21, D-79104 Freiburg i. Br., Germany

Received February 6, 1998; Revised Manuscript Received June 8, 1998

ABSTRACT: 50/50 wt % blends of isotactic polypropene (i-PP) with metallocene-based random poly(ethene-*co*-1-butene) (PEB) were prepared with 1-butene content varied from 52 to 100 wt %. The melt miscibility of the i-PP/PEB blends as a function of 1-butene content was studied by investigating the morphologies of the blends in the solid state by phase-imaging tapping mode atomic force microscopy (AFM) and transmission electron microscopy (TEM). It was found that i-PP is melt miscible with PEB for 1-butene contents of ≈88 wt % (miscibility window). Differential scanning calorimetry (DSC) analysis showed a slower and hindered i-PP crystallization in the miscible or partially miscible blends. Intensive investigations on the apparently one-phase blend were performed by optical microscopy, small-angle X-ray scattering and dynamic mechanical analysis.

Introduction

Blending isotactic polypropene (i-PP) with elastomeric ethene/1-olefin copolymers, e.g., ethene/propene or ethene/propene/diene, is known to improve the impact resistance of i-PP.[1] The key requirement for toughness enhancement is adequate compatibility between polypropene and ethene copolymer. Miscibility leads to highly flexible polypropene blends, while compatible two-phase blends can exhibit an attractive combination of stiffness and toughness. The compatibility or miscibility of an elastomeric olefin copolymer with i-PP depends strongly upon the molecular microstructure, such as monomer structure, chain stiffness, and energetic asymmetries.[2−8] Novel families of single-site metallocene-based Ziegler−Natta catalysts produce very uniform copolymers and give excellent control of copolymer molecular and supermolecular architectures. Characteristic features of metallocene-based copolymers are narrow molecular weight distribution ($M_w/M_n = 2$) and uniform comonomer incorporation covering the entire feasible composition range. Moreover, comonomer incorporation does not adversely affect high molecular weight. The conventional Ziegler−Natta catalysts give rather complex product mixtures containing homopolymers, high molecular weight copolymers with low comonomer content, and waxlike copolymers with high comonomer content. Therefore, metallocene catalysts produce excellent ethene/1-olefin model copolymers, e.g. poly(ethene-*co*-1-propene), 1-butene, 1-hexene, 1-octene, and long-chain 1-olefins, e.g. 1-hexadecene. In this study we used poly(ethene-*co*-1-butene) (PEB)/i-PP as a model system to investigate its miscibility behavior and elucidate the influence of PEB molecular architectures on phase separation and morphology development. In contrast to ethene/1-propene copolymers, ethene/1-butene copolymers exhibit lower glass transition temperatures and improved compatibility with i-PP.

Prior to the development of modern metallocene catalysts, ethene/1-butene copolymers were first synthesized by hydrogenation of polybutadiene containing different proportions of 1,4- and 1,2-units. Polybutadienes were available via anionic polymerization. Such hydrogenated products are referred to as poly(ethylene-*co*-ethylethylene) (PEE) in the literature.[9] They represent model random copolymers containing 1-butene rich atactic sequences. Modern metallocene catalysts copolymerize ethene with 1-butene over the entire feasible composition range from 100% ethene to 100% 1-butene. Depending on the structure of the metallocenes, the resulting copolymers can be atactic or stereoregular.[10] Here, PEB was prepared by using an isospecific metallocene catalyst.

Recently it has been reported that 1-butene rich PEE should be "miscible" with i-PP.[11] Small angle neutron scattering measurements showed a miscibility window of i-PP with PEE for PEE containing 73−90 wt % 1-butene. It should be noted, however, that the miscibility may be affected by the 1-butene sequences of PEE and PEB as well as by different stereoregularities. Such influences of stereoregularity on miscibility are well-known for stereoisomer blends. For example, i-PP is not miscible with syndiotactic PP in the melt.[12] A compatibility study of i-PP with poly(ethene-*co*-1-olefin) showed, that PEB with 56 and 62 mol % 1-butene content exhibited a better compatibility with i-PP in mechanically mixed melt blends than PEB with a smaller 1-butene content.[13] These blends exhibited "fairly homogeneous" morphologies, as determined by transmission electron microscopy (TEM), and a single glass transition temperature (T_g), as determined by dynamic-mechanical analysis (DMA).[13] It is important to note that a commercial grade i-PP with 3.2 wt % ethene incorporation was used in this study instead of a homopolymer i-PP.[13] Homopolymer i-PP should show a different behavior, however, because comonomer incorporation affects sensitively the miscible window. Blends of i-PP with PEB containing more than 62 mol % 1-butene have not been investigated in this study. Cham et al. investigated the miscibility of i-PP with isotactic poly(1-butene) (i-P1B) showing that i-PP is partially miscible with i-P1B.[14] To our knowledge, the morphologies of blends of i-PP with metallocene-based PEB covering the entire 1-butene content between 50 and 100 wt % have not been studied systematically yet.

S0024-9297(98)00179-X CCC: $15.00

Table 1. Some Chemical and Physical Properties of Poly(1-butene) and Poly(ethene-*co*-1-butene)

	sample				
	PEB52	PEB70	PEB82	PEB88	P1B
F [E] (wt %)[a]	48	30	18	12	0
F [B] (wt %)[a]	52	70	82	88	100
M_n[b]	82 800	62 400	63 500	82 100	46 700
M_w/M_n[b]	2.4	2.4	2.4	2.4	2.8
T_m (°C)[c]					97.7
T_g (°C)[d]	−57.9	−45.5	−41.4	−39.5	−15.2

[a] Determined by ^{13}C-NMR. [b] Determined by GPC using poly(ethene) standards. [c] Determined by DSC, heating rate 20 K/min. [d] Determined by DMA.

In the present work we examine the melt miscibility of i-PP with metallocene-based PEB as a function of the 1-butene content. The room-temperature morphologies of the 50/50 wt % i-PP/PEB blends were studied by tapping mode atomic force microscopy (AFM), TEM, and optical microscopy. The lamellar crystal morphology in the apparently melt one-phase blends was analyzed using small-angle X-ray scattering (SAXS) in combination with AFM.

Experimental Section

Materials and Blend Preparation. The i-PP used in this study was obtained from BASF AG. It has a number molecular weight $M_n = 87.1 \times 10^3$ $M_w/M_n = 2.95$, and a melt temperature $T_m = 166$ °C. PEB with various 1-butene contents was synthesized using methylaluminoxane-activated metallocene *rac*-$Me_2Si(2\text{-}MeBenz[e]Ind)_2ZrCl_2$ (MBI) catalysts, as described previously.[31] Table 1 summarizes some important chemical and physical properties of the PEB and i-P1B used in this study. Blends of i-PP with PEB52, PEB70, PEB82, PEB88, and i-P1B were prepared. The number associated with PEB indicates the weight percent content of 1-butene, which was varied from 52, 70, 82, 88, to 100 wt %.

i-PP/PEB blends of composition 50/50 wt % were prepared by mixing both components in a solution of xylene at 180 °C. The transparent hot solution was precipitated into cold acetone, filtered, and then dried in air for more than two weeks. The solvent free blends were then heated to 180 °C and annealed under vacuum for 5 h. From all the blends prepared in the melt only the i-PP/PEB88 blend was transparent and homogeneous. For AFM and TEM measurement the samples were annealed in the melt and then cooled from 180 °C down to room temperature using a cooling rate of 10 K min^{-1}.

Atomic Force Microscopy. AFM experiments were performed with a Nanoscope III scanning probe microscope. The height and phase images were obtained simultaneously while the instrument was operated in the tapping mode under ambient conditions. We used commercial Si cantilevers with force constants of 13−70 N/m. Images were taken at the fundamental resonance frequency of the Si cantilevers, which was typically around 300 kHz. Typical scan speeds during recording were 0.3−1 line/s using scan heads with a maximum range of 170 × 170 μm or 16 × 16 μm. All images were taken with a driving amplitude $A_0 \approx 60$ nm and a set-point amplitude $A_0 \approx 40-48$ nm. The phase images represent the variations of relative phase shifts (i.e., the phase angle of the interacting cantilever relative to the phase angle of the freely oscillating cantilever at the resonance frequency). For AFM measurements the blends were annealed at 180 °C for 5 h and then cooled to room temperature at a rate of 10 °C min^{-1}. The flat surfaces that were examined were obtained by cutting the sample with a Diatome diamond knife at ≈−45 °C using an ultramicrotome (Ultracut E, Reichert & Jung) equipped with a cryochamber.

Transmission Electron Microscopy (TEM). The TEM measurements were carried out with a Zeiss CEM 902 transmission electron microscope applying an acceleration voltage of 80 keV. The specimens were prepared using an ultramicrotome (Ultracut E, Reichert & Jung) equipped with a cryochamber. Thin sections of about 100 nm were cut with a Diatome diamond knife at −40 °C. The samples were stained with RuO_4.

Light Microscopy. The optical micrographs were taken with an Olympus-Vanox AH2 microscope with crossed polarizators. Samples for the light microscopy were prepared by melting the precipitated and dried material between two cover glass plates. The layer thickness between the glass plates was about 20−50 μm. The samples were annealed at 180 °C for 5 h and then quenched to crystallization temperature at 150 °C.

Wide-Angle X-ray Scattering (WAXS). For WAXS measurements the samples were prepared as described above. After the thermal treatment the samples were cooled from 180 °C to room temperature with a cooling rate of 0.2 °C/min. The WAXS experiments were carried out with a Siemens D500 apparatus. For all measurements the Cu Kα radiation with a wavelength $\lambda = 0.154$ nm was used.

Small-Angle X-ray Scattering (SAXS). For SAXS measurements the samples were isothermally crystallized from the melt at 130 °C for 2 h for i-PP and for 24 h for the i-PP/PEB88 blend under vacuum. The SAXS measurements were performed in an evacuated Kratky compact camera (Anton Paar K. G.) with an 80 μm entrance slit. Cu Kα radiation with a wavelength of $\lambda = 0.154$ nm was used. The scattered intensity (I) was recorded with a scintillation counter in a step-scanning mode at 130 °C.

Dynamic Mechanical Analysis (DMA). The DMA measurements were carried out with a Rheometrics RSA II solid analyzer. The heating rate was 3 °C min^{-1}.

Differential Scanning Calorimetry (DSC). DSC measurements were carried out with a Perkin-Elmer DSC 7 apparatus. The samples were cooled from the melt with a rate of 10 °C min^{-1} and then heated to 180 °C with a heating rate of 20 °C min^{-1}.

Results and Discussion

First, the PEB samples with various 1-butene contents were investigated by WAXS to obtain information about their stereoregularity and crystallizability. Figure 1 shows the WAXS diagrams for PEBs with various 1-butene contents. The peaks at 2θ of 10.1, 17.5, 20.3, and 20.6° were distinguished as typical reflections for crystalline isotactic P1B, thus indicating that 1-butene sequences in the 1-butene rich copolymers are isospecific.[15] As the 1-butene content is lowered, these peaks become smaller and disappear finally, which indicates that with decreasing 1-butene content, the crystallizability of the copolymer decreases rapidly (Figure 1).

The morphologies and the nanostructures of the blend samples were primarily examined by AFM phase imaging. Figures 2a−e show AFM phase images of blends of i-PP with PEB52, PEB70, PEB82, PEB88, and i-P1B, respectively. Before investigation, the samples were annealed at 180 °C for 5 h (see Experimental Section) to obtain information about their equilibrium melt miscibility while analyzing the samples in the solid state. To study the bulk morphology rather than the surface morphology, the images were recorded on surfaces that were obtained by cutting the samples with an ultramicrotome. The dark regions in the AFM phase images can be assigned to the PEB rich phase and the bright regions to the i-PP rich phase. This assignment is based on the considerations given below (detailed discussion of AFM phase image contrast formation is not the purpose of the present work; however, the reason for this assignment should be addressed in a few words).

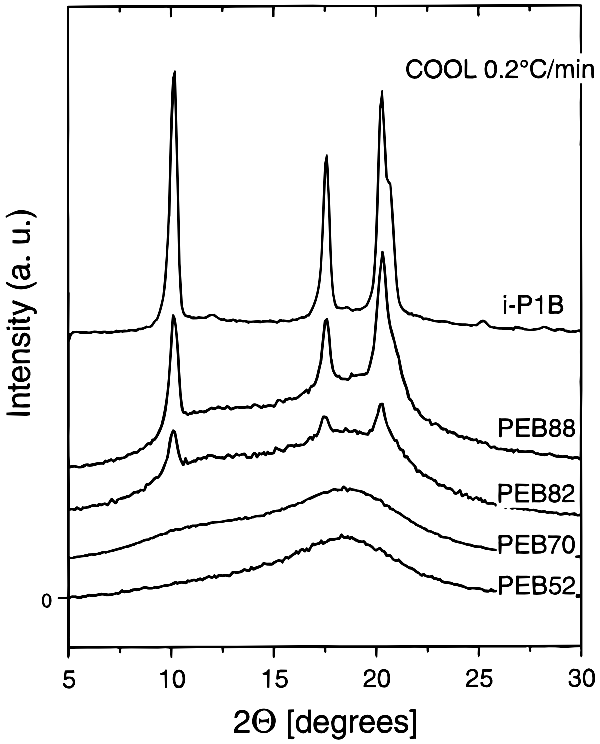

Figure 1. WAXS diagrams of PEBs with different 1-butene contents. The numbers associated with the PEB inscription indicate the weight percent content of 1-butene.

Phase imaging is a relatively new extension of tapping mode AFM. In tapping mode AFM the cantilever oscillates vertically near its resonance frequency, so that the tip makes contact with the sample surface only briefly in each cycle of oscillation. The short, intermittent tip−sample contact avoids lateral forces during scanning and prevents sample damage. As the tip is brought close to the sample surface, the vibrational characteristics (i.e., the force constant, resonance frequency, phase angle, and amplitude) of the cantilever change due to the tip−sample interaction. Phase detection allows one to detect shifts in phase angles of vibration when the oscillating cantilever interacts with the sample surface.[16] Phase imaging (i.e., image contrast related to the phase shifts) has been shown to provide enhanced image contrasts, especially for heterogeneous surfaces.[17−21] The contrasts of tapping mode AFM height and phase images depend in a complex way on the driving amplitude A_0 and the set-point ratio $r_{sp} = A_{sp}/A_0$ of the cantilever.[19,21−27] For large A_0, moderate and small r_{sp}, the tip−sample interaction becomes repulsive so that the phase image contrast is related to the variation of the local surface stiffness on the sample surface. In this case, a larger stiffness leads to a more positive phase shift and thus to a brighter contrast in the phase image. However, when A_0 is small and the sample is very soft, the tip−sample interaction can be dominated by attractive forces. In this case, adhesion and capillary forces lead to a negative phase shift. Furthermore, for soft samples the contribution of viscous damping has to be considered. Especially when A_0 is small, the contact time of the tip interacting with the sample becomes larger. As a result, the cantilever's vibrational characteristics may be strongly affected by the viscous damping. Consequently, the phase image contrast may be reversed for small A_0. The images presented here were all recorded at moderate amplitudes $A_0 \approx 60$ nm and typical set-point amplitudes $A_{sp} \approx 40-48$ nm. The conditions under which the images were taken led to an average most positive phase shift in the bright regions, which can be thus assigned to i-PP. Since the PEB component is by far more compliant, we assign the regions with the most negative phase shift to the PEB component, corresponding to the image regions with dark contrast.

Figure 2a shows the AFM phase image of i-PP/PEB52. Large, irregular domains of bright and dark contrast can be distinguished. According to the discussion above, the areas of bright contrast can be assigned to the i-PP rich phase and the areas of dark contrast to the PEB rich phase. The size of the irregularly formed i-PP domains is up to several tens of micrometers in diameter. Figure 2b shows the AFM phase image of i-PP/PEB70. Direct comparison of the AFM images displayed in Figure 2a,b reveals that the domain size decreases significantly as the amount of 1-butene content is increased from 52 to 70 wt %. The size of the PEB rich domains does not exceed 2 μm in diameter and can be as small as 200 nm in diameter (Figure 2b). Figure 2c shows the AFM phase image of i-PP/PEB82. Clearly, the further increased 1-butene content results in a further decrease of the size of the PEB rich domains of dark contrast embedded in the i-PP matrix of bright contrast. The size of these PEB rich domains in Figure 2c is typically in the range of ≈200 nm. As the 1-butene content of the PEB component is further increased to 88 wt %, no phase separation of the i-PP and PEB phases can be observed. This is demonstrated in Figure 2d, which shows the AFM image of i-PP/PEB88. The small structures observed in this image are practically indistinguishable from structures that might be induced by the knife used to obtain the flat surfaces (see discussion below). Finally, Figure 2e shows the AFM image of i-PP/i-P1B. Two phases can be distinguished, both showing a crystalline structure. The crystalline structures of these two separate phases show differences that can be the result of differences in their crystalline morphologies. The component showing the coarse grain structure can be most likely assigned to the i-PP rich phase due to its similarity to i-PP rich phases found in other i-PP blends. It should be noted that AFM phase imaging is very sensitive to differences in polymer stiffness and crystallinity. As shown in Figure 1, the crystallinity of PEB decreases rapidly when the 1-butene content is decreased. i-P1B exhibits a crystallinity comparable to i-PP (about 60%) and, consequently, the phase images of the i-PP/i-P1B blends show only weak contrast (Figure 2e). PEB88, however, exhibits much lower crystallinity (about 33%) compared to i-PP and i-P1B. Consequently, the phase image contrast between the i-PP rich and the PEB88 rich regions should be large and easy to detect. Thus, the AFM image shown in Figure 2d demonstrates that the i-PP/PEB88 blend apparently exhibits no phase separation.

The same blend samples were also studied by TEM, which is the conventional method to study polymer morphologies with high magnification. The TEM images revealed essentially identical morphologies as the AFM phase images. As a representative example, Figure 3 shows the TEM image obtained for the i-PP/PEB82 sample. The TEM image reveals the same phase-separated morphology as the AFM phase image (Figure 2c). The regions of dark contrast can be assigned to the PEB82 rich phase (as a result of staining

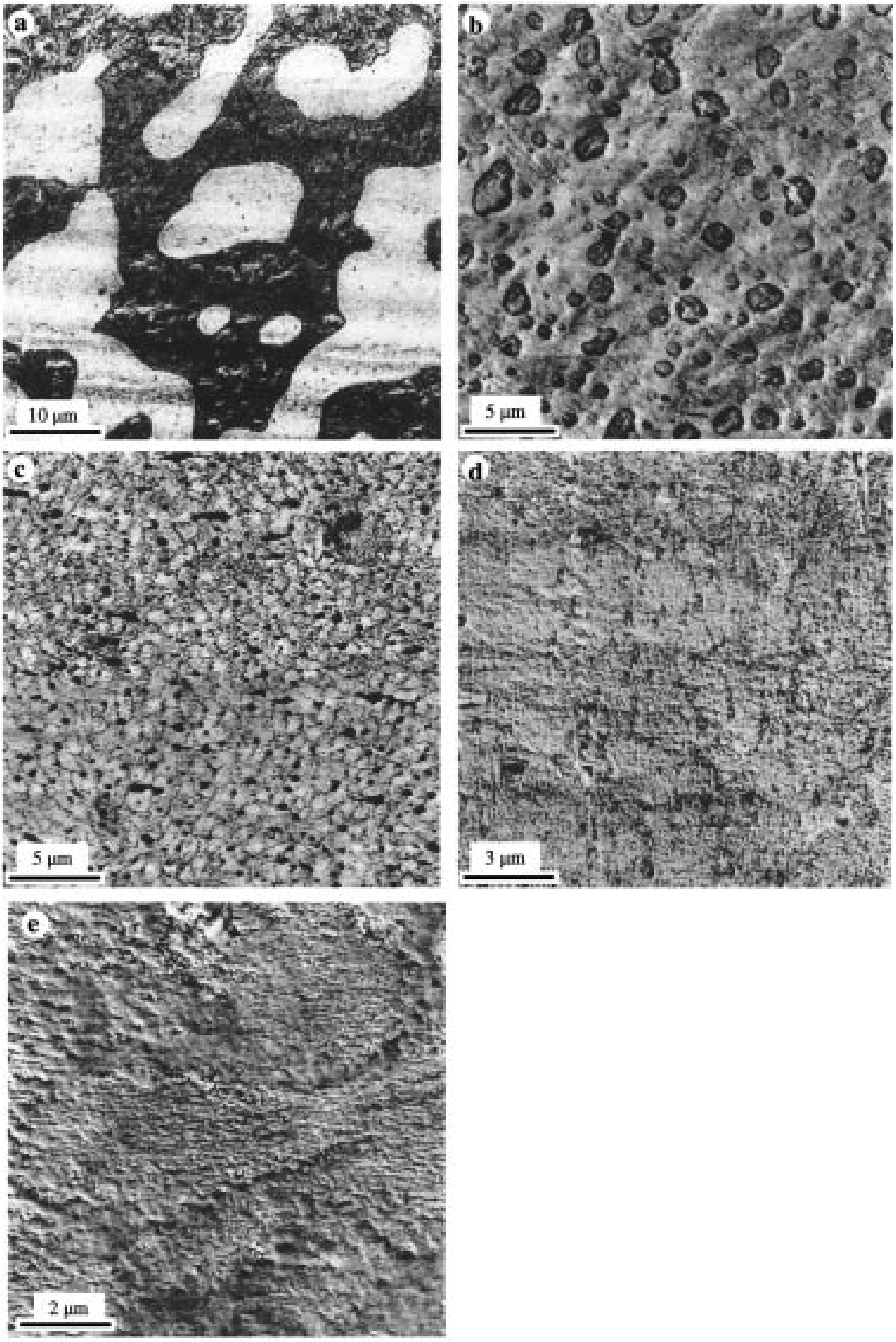

Figure 2. AFM phase images of i-PP/PEB blends: (a) i-PP/PEB52, (b) i-PP/PEB70; (c) i-PP/PEB82; (d) i-PP/PEB88; (e) i-PP/i-P1B. The contrast covers phase angle variations in the 120° range in (a), in the 180° range in (b)−(d), and in the 45° range in (e).

with RuO_4) and the regions of bright contrast to the i-PP rich phase. At higher magnification a very defuse interface of about 100 nm width between the PEB82 rich regions and the i-PP rich regions is observed (Figure 3b). This can be assigned to the relatively wide concentration gradient of i-PP and PEB82 at the interface, which may occur during i-PP crystallization in the i-PP rich phase upon cooling. It should be noted that the width of the interface region (100 nm) is relatively large compared to the i-PP lamellae thickness (≈25 nm), which can be distinguished in the TEM image. Therefore, it is very likely that the diffuse interface is caused by a relatively wide concentration gradient of i-PP and PEB82 at the interface and is not a limitation of the ability to resolve structures when using RuO_4 is used as staining agent.

It is an important observation that TEM images are essentially identical with the AFM phase images, both using the same sectioning procedure. It should be noted, however, that TEM requires very thin sample sections of uniform thickness. For AFM studies the flat surfaces obtained by microtomy can be used, and

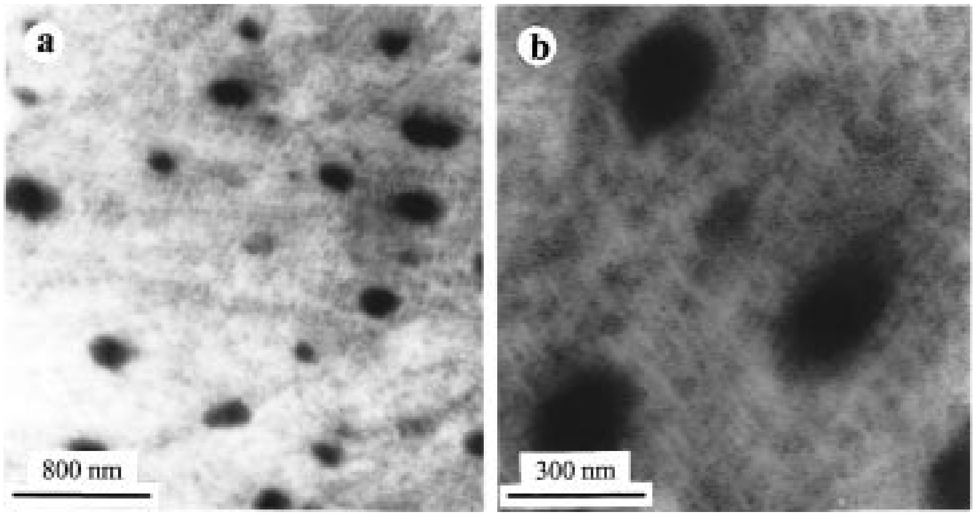

Figure 3. TEM images of the i-PP/PEB82 blend at two different magnifications.

variations of sample thickness are not relevant, making sample preparation rather easy compared to TEM. Thus, the material-related contrast as observed in Figure 2 demonstrates that AFM phase imaging provides an interesting and powerful alternative to TEM for morphology studies of polymers.

The AFM images displayed so far were recorded on surfaces that were obtained by cutting the blends using a diamond knife. As mentioned above, this preparation procedure results in small structures and some roughness on the surface. Such structures are affected by several parameters such as the material, knife quality, and cutting temperature. In the case of the i-PP/PEB blends under investigation it was impossible to obtain completely smooth surfaces down to the nanometer scale. The structures induced by the cutting procedure showed typical dimension of 50−200 nm. From this it can be concluded that for these samples the morphologies with dimensions larger than the structures induced by the knife can be observed by AFM without further sample treatment. However, it is much more difficult to observe the nanoscale morphology and nanostructures of the i-PP/PEB88 sample because high-resolution images of features smaller than 300 nm are disturbed by structures induced by the knife.

To overcome this difficulty and to make an investigation of the nanostructures possible, the surface of the i-PP/PEB88 sample was treated by the following procedure. The sample was melted again at 180 °C for 20 min with the sample surface (as obtained by cutting) facing a cover glass. The sample was then crystallized at 130 °C for 24 h and subsequently quenched to room temperature. Finally, the sample was peeled from the cover glass and the film−glass interface was investigated by AFM. i-PP crystallizes at 130 °C while the low crystalline PEB88 melts around $\approx$60 °C. Thus, the crystalline morphology and structures resulting from this treatment should correspond to the i-PP component. For comparison, samples of pure i-PP were prepared using the same procedure and the resulting structures were examined by AFM.

Figure 4a and 4b show the AFM phase images of an i-PP/PEB88 sample surface that was treated as described above. The images exhibit lamellae and lamellae bundles that can be assigned to i-PP because of the much lower crystallinity of PEB88. The i-PP lamellar dimensions (long period) in the blend are typically in the range of 30−50 nm. For comparison Figure 4c shows the AFM phase image of a sample consisting of i-PP only, which was treated in an identical manner. The image shows a lamellar structure with interlamellar dimensions (long period) around 24 nm, which is similar to the results obtained by SAXS measurements for i-PP (see below). From the direct comparison of Figure 4b,c the difference in structure is evident. The lamellae and lamellae bundles are obviously separated by regions of amorphous material (Figure 4b). This separation is typically in the range 100−250 nm. It should be noted that the i-PP/PEB88 blend was annealed at 180 °C for 5 h without any observation of phase separation. Thus, it is very likely that the i-PP/PEB88 blend forms a single homogeneous phase in the melt. Upon cooling, i-PP crystallizes from the melt, growing as lamellae and tightly packed lamellae bundles. Consequently, we believe that the crystalline morphology observed in Figure 4a,b is the result of the growing process of one homogeneous single phase in the melt. Hence, 50/50 wt % i-PP/PEB88 blends are apparently miscible in the melt.

Parts a and b of Figure 5 show the optical micrographs of 50/50 wt % i-PP/PEB88 blend and i-PP, respectively, after annealing at 180 °C for 5 h under vacuum and crystallization at 150 °C. For i-PP/PEB88 the observed crystalline spherulites are much larger than for i-PP. This can be explained by the slower nucleation and crystal growing rate observed for i-PP/PEB88 (the time needed for complete crystallization was 20 h for i-PP/PEB88 and 10 h for i-PP). Similar evidence was found for other miscible i-PP blend systems.[28] The slow nucleation and crystal growing rate, and the uniform growth of i-PP spherulites in the blend support also the conclusion that PEB88 and i-PP are miscible in the melt.

According to investigations by Cham et al.,[14] i-PP and i-P1B should be partially miscible. The morphology and structure displayed in Figure 2e, however, makes it difficult to decide whether i-PP is incorporated in both phases. To explore this problem in more detail, the same sample (Figure 2e) was further treated as follows to remove the i-P1B phase from the surface. The sample was melted again at 180 °C for a few minutes with the sample surface (as obtained by cutting) facing a cover glass. The sample was then crystallized at a temperature of 155 °C under vacuum for 3 days, cooled to room

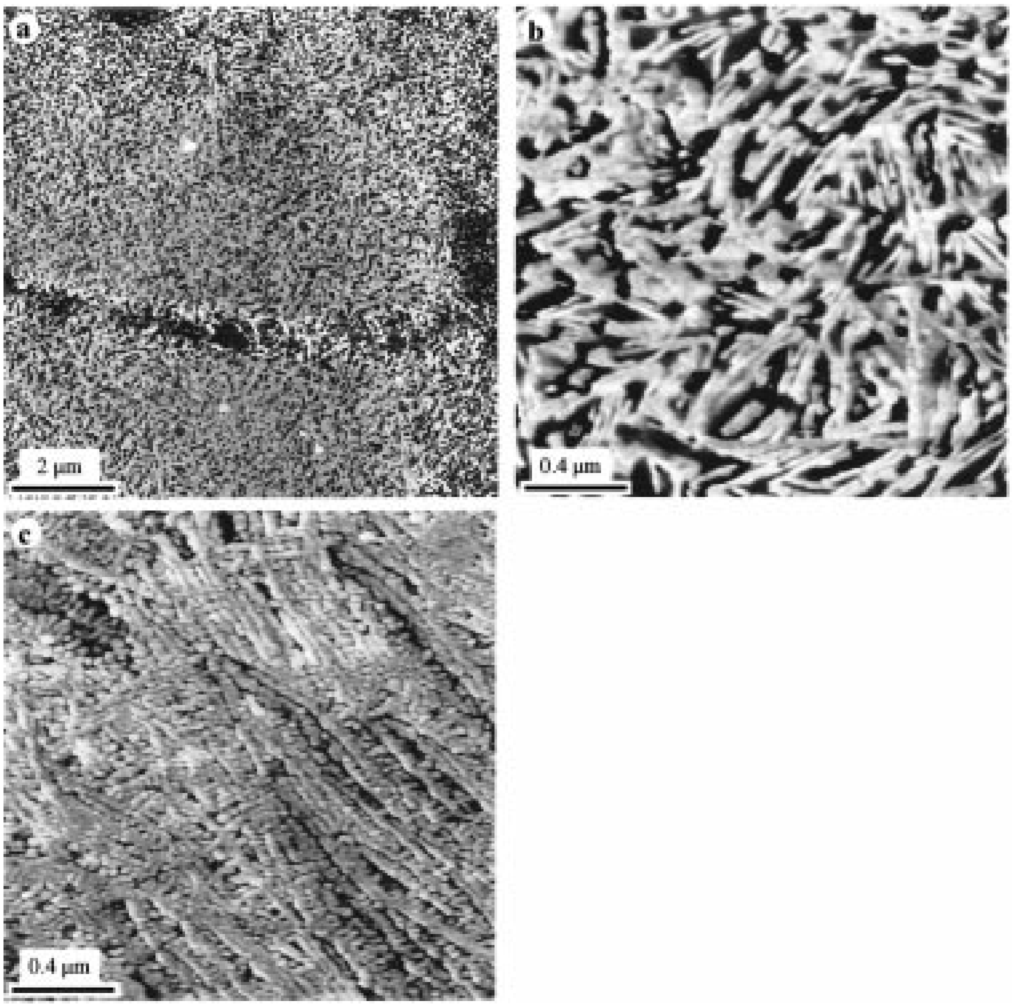

Figure 4. AFM phase images of the i-PP/PEB88 blend. (c) AFM phase image of i-PP. The contrast covers phase angle variations in the 140° range in (a) and in the 180° range in (b) and (c).

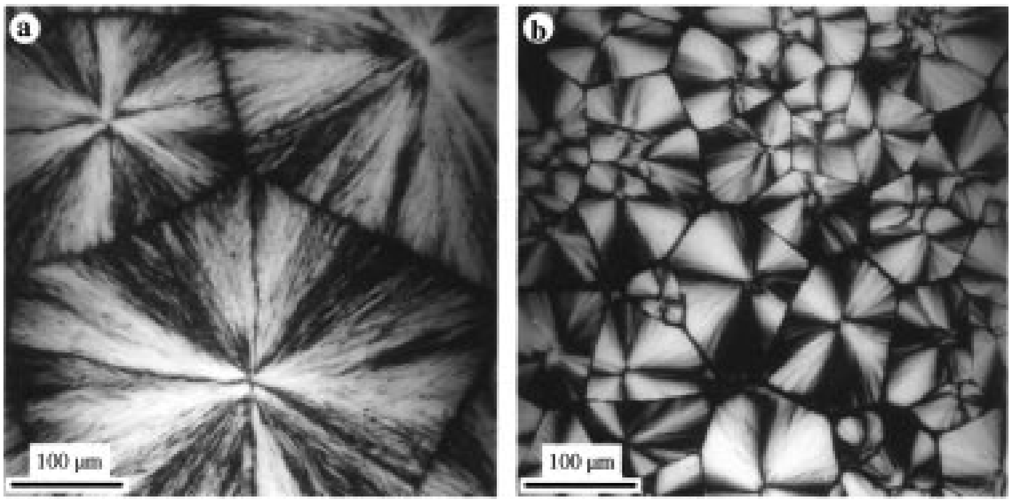

Figure 5. (a) Polarized optical micrograph of the i-PP/PEB88 blend. (b) Polarized optical micrograph of i-PP.

temperature, and peeled from the glass surface. Then, the sample was annealed again at 155 °C for 4 h under vacuum; however, the previous sample−glass interface being this time at the vacuum interface. As a result of this procedure the i-P1B component melts and flows down from the sample surface, whereas the i-PP crystal remains almost unchanged at the surface (the crystallization at 155 °C for 3 days is sufficiently long for a complete crystallization such that melting of i-PP will not occur when the sample is again heated to this temperature). Using a reflection optical microscope, two surface regions exhibiting two different crystalline morphologies were identified. One surface region is characterized by tightly grown spherulites with sharp, clearly distinguishable borders between the spherulites, the other surface region exhibits a coarse texture without well-defined borders between the spherulites. Parts a and b of Figure 6 show AFM height images that

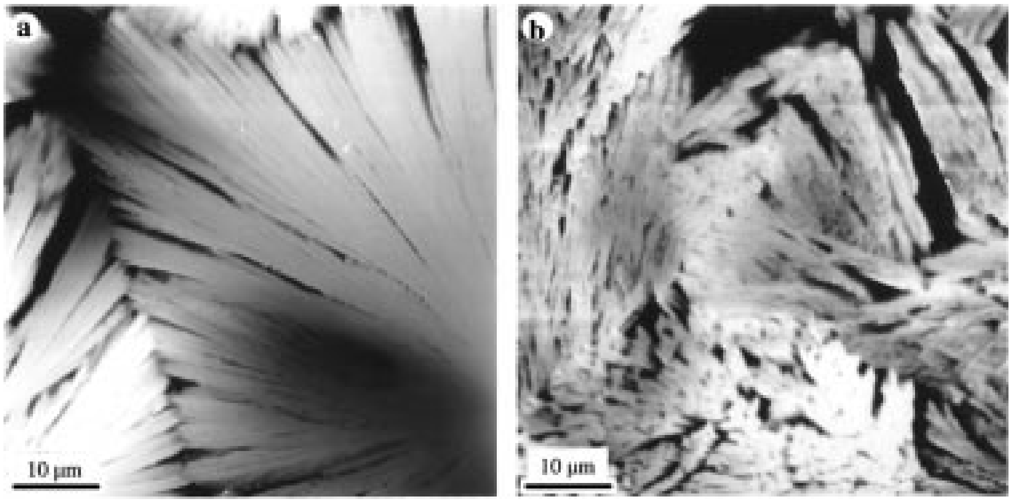

Figure 6. AFM height images of the i-PP/i-P1B blend obtained on the two surface regions that can be distinguished in Figure 2e. The contrast covers height variations in the 2 μm range in (a) and (b).

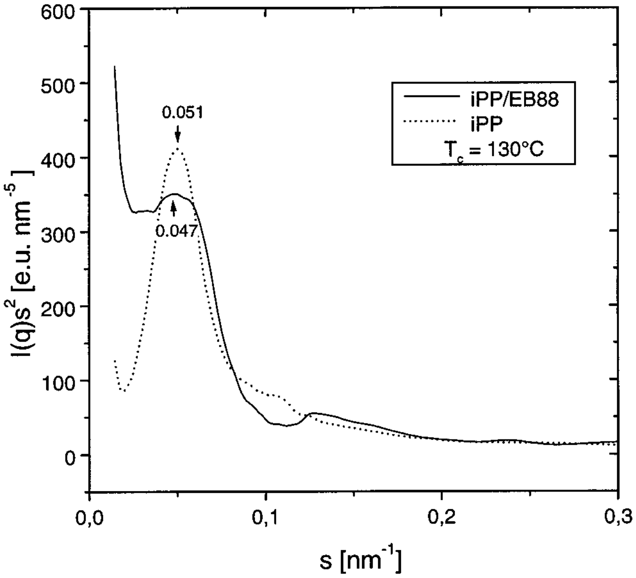

Figure 7. SAXS spectra of the i-PP/PEB88 blend (solid line) and i-PP (dotted line).

were taken on these two different surface regions, respectively. From the morphology observed in Figures 6a,b it is obvious that i-PP is incorporated in both phases of the i-PP/i-P1B blend.

On the basis of the above findings, we conclude that among the PEBs studied here only PEB88 is fully miscible with i-PP. In contrast, PEB containing less than 88 wt % 1-butene was found to be partially miscible or immiscible with i-PP, depending on the 1-butene content. i-P1B (i.e., 100 wt % contents of 1-butene) was found to be partially miscible with i-PP. This is in agreement with the observations by Cham et al.[14] Therefore, we estimate the miscibility window for PEB in i-PP/PEB blends around 88 wt % 1-butene content.

The crystalline bulk morphology of the i-PP/PEB88 blend was further investigated by SAXS measurements. The SAXS data were taken at a temperature of 130 °C. At this temperature i-PP crystallizes but PEB88 does not. SAXS measurements were also performed for i-PP samples to compare the crystalline structure of the i-PP/PEB88 blend with that of i-PP. Figure 7 shows the obtained SAXS data which display $I(q)s^2$ versus s, where $I(q)$ is the intensity function, $q = (4\pi/\lambda)\sin\theta$ and $s = (2/\lambda)\sin\theta$, where θ is the scattering angle. From the obtained i-PP data only $I(q)/2$ was used for comparison with the i-PP/PEB88 data because the i-PP/PEB88 blend contains 50 wt % i-PP. The maxima in the SAXS diagrams (marked by arrows) can be assigned to the average size of the lamellae and amorphous regions, i.e., interlamellar distances. As can be seen in Figure 7, the SAXS diagram of i-PP shows a sharp and symmetric peak around $s \approx 0.050$ nm^{-1}, which corresponds to a long period $d \approx 20$ nm. The SAXS data of i-PP/PEB88, however, display a much broader and smaller peak around $s \approx 0.045$ nm^{-1}, which corresponds to a long period of 21.3 nm. Moreover, the SAXS diagram of i-PP/PEB88 shows a plateau located at the left side of the maximum. This plateau can be assigned to a long period having a broad distribution in the range of 30−50 nm, which is in agreement with the AFM measurements.

The SAXS measurements of i-PP/PEB88 give us some insight into the crystalline morphology of the i-PP/PEB88 blend. From the SAXS data it can be concluded that most of the lamellae are packed into compact bundles having an interlamellar distance of 21.3 nm, which is close to the interlamellar distance found for pure i-PP. However, some lamellae are obviously packed loosely, exhibiting a broad distribution of interlamellar distances in the range 30−50 nm. Thus, a considerable amount of PEB88 must reside in the region between the lamellae. Since the i-PP/PEB88 blend contains 50 wt % of PEB88, it is obvious that not all PEB88 can be located in the region between the lamellae. Therefore, we conclude that a large amount of PEB88 forms pockets between lamellae bundles, as described for other melt miscible blends.[29,30] AFM measurements have shown that the size of this pocket is around 100 nm, which could not be detected by SAXS measurements. The maximum in the SAXS diagram of the blend indicates that much more compact lamellar bundles are present in the bulk than at the sample−glass interface investigated by AFM.

The difference between the observed lamellar compactness in bulk and at the sample−glass interface can be explained by the different mobilities of the two polymers species during the crystal growth. It is known that the exclusion of noncrystalline polymer from the interlamellar region in a melt miscible crystallizable/noncrystallizable polymer blend is strongly affected by

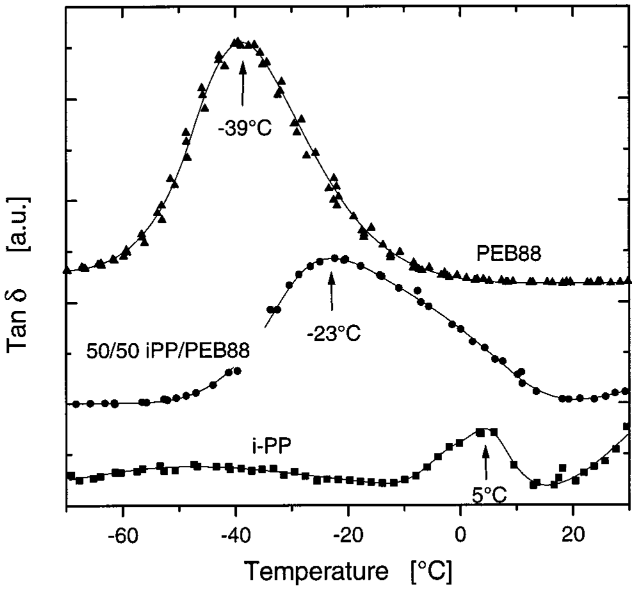

Figure 8. Variation of the loss tangent (tan δ) as a function of temperature for the i-PP/PEB88 blend and the blend components, PEB88 and i-PP. The arrows indicate the corresponding glass transition temperature.

the mobility of noncrystalline polymer during crystallization. Larger mobility of a polymer leads to a larger and easier exclusion of the amorphous polymer during crystal growth, which results in more compact lamellae. Because of geometrical limits the polymer mobility at the glass interface is evidently smaller than that in the bulk, which could explain the more compact lamellae bundles in the bulk compared to the sample–glass interface.

Figure 8 shows the DMA data obtained for the i-PP/PEB88 blend and for the blend components (i.e., PEB88 and i-PP). The temperature dependence of tan δ for the i-PP/PEB88 blend, PEB88, and i-PP shows that tan δ has a peak at 5 °C for i-PP, at −39 °C for PEB88, and a single peak at −23 °C for i-PP/PEB88. Although the loss tangent tan δ shows a shoulder on the right side of the i-PP/PEB88 peak, one can use the Fox equation to exclude that this asymmetric peak is the result of two overlapping peaks. According to the Fox equation the glass transition temperature T_g for a miscible blend is given by

$$\frac{1}{T_g} = \frac{w_1}{T_{g1}} + \frac{w_2}{T_{g2}}$$

where T_{g1}, T_{g2}, w_1, and w_2 are the glass transition temperatures and mass fractions of components 1 and 2, respectively. Taking into account the crystallinity of i-PP ($\approx$60%) and PEB ($\approx$33%), the calculated glass transition temperature according to the Fox equation should be $\approx$−25 °C, which is very close to our experimental value. The observation of the shoulder on the right side of the peak can be the effect of i-PP crystallization from the melt and due to the formation of a pocket structure as discussed above (see discussion of SAXS data above). The observation of a single glass transition temperature and its strong shift for i-PP/PEB88 provides additional experimental evidence that i-PP is fully miscible with PEB88 in the melt.

Figure 9 shows the DSC diagrams recorded for all of the blends investigated in this study (some transitions at lower temperatures, most likely corresponding to melting of i-PP in the PEB rich phase or from melting of crystallizable PEB, are not included). The samples were cooled from +180 to −100 °C with a cooling rate of 10 °C·min^{-1} before taking the DSC heating curves (representative cooling curves for i-PP and i-PP/PEB88 are shown as insets in Figure 9). Figure 9 shows that the melting temperature is considerably reduced for the miscible and partially miscible blends. Since the equilibrium melting point for these miscible or partially miscible blends would not be expected to decrease significantly, the observed decrease of the melting point in Figure 9 should be the result of nonequilibrium melting of i-PP. As shown in Figure 5 and in the inset of Figure 9 slower nucleation and crystallization were observed for the miscible blend because of the incorporation of PEB. Thus, one can suspect that the origin of higher melting temperature for the i-PP/PEB52 blend is faster nucleation and crystallization of i-PP with very small incorporation of PEB52.

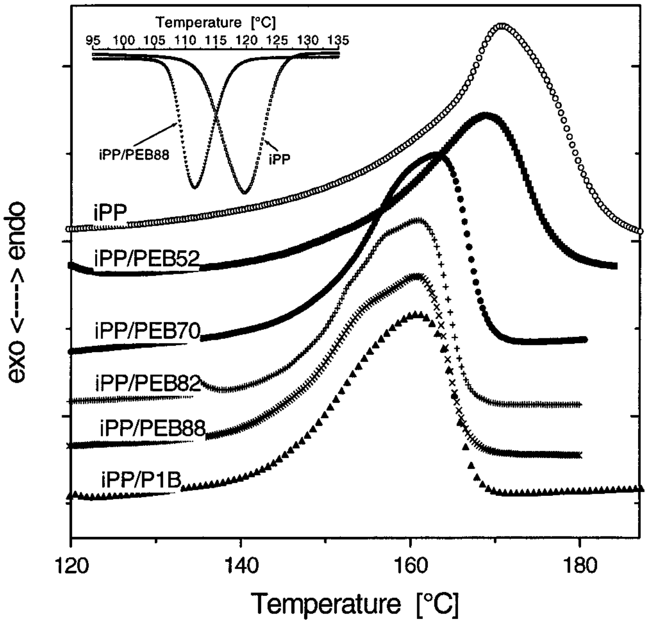

Figure 9. DSC curves obtained for i-PP and the i-PP/PEB blends. The heating rate was 20 °C min^{-1}. Prior to heating, the samples were crystallized by cooling from +180 to −100 °C with a cooling rate of 10 °C min^{-1} (the cooling curves for i-PP and i-PP/PEB88 are shown in the inset of Figure 9).

Conclusions

This study demonstrates that AFM phase imaging is a powerful tool for examination of morphology, nanostructure, and phase separation of polymer blends with excellent material related image contrast. The morphology observed in AFM phase images is in agreement with the findings observed in TEM studies, where the same microtomy procedure could be used for AFM well as for TEM, whereas for AFM no ultrathin sections and staining are needed.

The morphology of the 50/50 wt % i-PP/PEB blends depends strongly on the 1-butene content in PEB. When the 1-butene content in PEB was varied between 52 and 100 wt %, miscibility in the melt was found only for the i-PP/PEB blend with 88 wt % 1-butene content in PEB. SAXS data for the one-phase blend show a larger interlamellar distance than for i-PP and a pocket structure. The blends of i-PP with PEB82 and P1B showed partial miscibility. The miscibility window for i-PP/PEB was found to be smaller than that for i-PP/PEE blends.[11] The 1-butene content in PEB in the miscible i-PP/PEB blend was found to be larger than that reported by Yamaguchi et al. for i-PP with 3.2 wt % ethene comonomer content. The reason for the good miscibility of i-PP with PEB88 can be attributed to a match of chain stiffness and solubility parameters. This is in agreement with other experimental and theoretical reports.[2−8,11] The thermodynamics of i-PP/PEB blends is being investigated using the above-mentioned model polymers derived from metallocene catalysts.

Acknowledgment. We would like to thank Barbara Heck for collecting the SAXS spectra and Dr. Stühn for his advice and helpful discussions on interpretation of the SAXS data, both from the Faculty of Physics, Freiburg. Financial support was provided by the Deutsche Forschungsgemeinschaft (Sonderforschungsbereich 428) and by the Minister für Wissenschaft und Kultur von Baden-Württemberg (Schwerpunkt 29). The authors also thank the Bundesministerium für Bildung, Wissenschaft, Forschung und Technologie (BMBF) for supporting research on metallocene-catalyzed copolymer copolymerization as part of the BMBF project No. 03D0055.

References and Notes

(1) Moore, E. P., Jr., Ed. *Polypropylene Handbook*; Hanser Publishers: Munich, 1997. (b) van der Ven, S. *Polypropylene and other Polyolefins*; Elsevier: Amsterdam, 1990.
(2) Foreman, K. W.; Freed, K. F. *Macromolecules* **1997**, *30*, 7379.
(3) Graessley, W. W.; Krishnamoorti, R.; Balsara, N. P.; Butera, R. J.; Fetters, L. J.; Lohse, D. J.; Schulz, D. N.; Sissano, J. A. *Macromolecules* **1994**, *27*, 3896. (b) Krischnamoorti, J. R.; Graesley, W. W.; Balsara, N. P.; Lohse, D. J. *Macromolecules* **1994**, *27*, 3037.
(4) Schweizer, K. S. *Macromolecules* **1993**, *26*, 6050.
(5) Dudowitz, J.; Freed, F. *Macromolecules* **1991**, *24*, (a) 5076, (b) 5096.
(6) Bates, F. S.; Fredrickson, G. H. *Macromolecules* **1994**, *27*, 1065. (b) Fredrickson, G. H.; Liu, A. J.; Bates, F. S. *Macromolecules* **1994**, *27*, 2503.
(7) Jo, W. H.; Lee, M. S. *Macromolecules* **1992**, *25*, 842.
(8) Bates, F. S.; Kumar, A.; Schulz, M. F. *Macromolecules* **1995**, *28*, 1423.
(9) Rachapudy, H.; Smith, G. G.; Raju, U. R.; Graessley, W. W. *J. Polym. Sci., Polym. Phys. Ed.* **1979**, *17*, 1211.
(10) Tritto, I.; Fan, Z. Q.; Locatelli, P., Sacchi, M. C.; Camurati, I.; Galimberti, M. *Macromolecules* **1995**, *28*, 3342.
(11) Weimann, P. A.; Jones, T. D.; Hillmyer, M. A.; Bates, F. S.; Londono, J. D.; Melnichenko, Y.; Wignall, G. D.; Almdal, K. *Macromolecules* **1997**, *30*, 3650.
(12) Thomann, R.; Kressler, J.; Setz, S.; Wang, C; Mülhaupt, R. *Polymer* **1996**, *37*, 2627, 2635.
(13) Yamaguchi, M.; Miyata, H.; Nitta, K.-H. *J. Appl. Polym. Sci.* **1996**, *62*, 87.
(14) Cham, P. M.; Lee, T. H.; Marand, H. *Macromolecules* **1994**, *27*, 4263.
(15) Luciani, L.; Seppälä, J.; Löfgreen, B. *Prog. Polym. Sci.* **1988**, *13*, 37.
(16) Chernoff, D. A. *Proceedings Microscopy and Microanalysis*, San Francisco Press: San Francisco, 1995.
(17) Magonov, S. N.; Elings, V.; Papkov, V. S. *Polymer* **1997**, *38*, 297.
(18) Leclère, Ph.; Lazzaroni, R.; Brédas, J. L.; Yu, J. M.; Dubois, Ph.; Jèrôme, R. *Langmuir* **1996**, *12*, 4317.
(19) Bar, G.; Thomann, Y.; Brandsch, R.; Cantow, H.-J.; Whangbo, M.-H. *Langmuir* **1997**, *13*, 3807.
(20) McMaster, T. J.; Hobbs, J. K.; Barham, P. J.; Miles, M. J. *Probe Microsc.* **1997**, *1*, 43.
(21) Magonov, S. N.; Elings, V.; Whangbo, M.-H. *Surf. Sci. Lett.* **1997**, *375*, L385.
(22) Thomann, Y.; Cantow, H.-J.; Bar, G.; Whangbo, M.-H. *Appl. Physics A* **1988**, *A66*, S1233.
(23) Winkler, R. G.; Spatz, J. P.; Sheiko, S.; Möller, M.; Reineker, P.; Marti, O. *Phys. Rev. B* **1996**, *54*, 8908.
(24) Sarid, D.; Ruskell, T. G.; Workman, R. K.; Chen, D. *J. Vac. Sci. Technol. B* **1996**, *14*, 864.
(25) Anczykowski, B.; Krüger, D.; Fuchs, H. *Phys. Rev. B* **1996**, *53*, 15485.
(26) Burnham, N. A.; Behrend, O. P.; Oulevey, F.; Gremaud, G.; Gallo, P.-J.; Gourdon, D.; Dupas, E.; Kulik, A. J.; Pollock, H. M.; Briggs, G. A. D. *Nanotechnol.* **1997**, *8*, 67.
(27) Brandsch, R.; Bar, G.; Whangbo, M.-H. *Langmuir* **1997**, *13*, 6349.
(28) Yamaguchi, M.; Miyata, H.; Nitta, K.-H. *J. Polym. Sci.* **1997**, *35*, 953.
(29) Saito, H.; Stühn, B. *Macromolecules* **1994**, *27*, 216.
(30) Chang, H. L.; Okada, T.; Saito, H.; Inoue, T. *Polymer* **1997**, *38*, 31.
(31) Schneider, M. J.; Suhm, J.; Mülhaupt, R.; Prosenc, M.-H.; Brintzinger, H.-H. *Macromolecules* **1997**, *30*, 0, 3164.

MA980179M